

1 Characteristics of the summer atmospheric boundary layer height 2 over the Tibetan Plateau and influential factors

3 Junhui Che^{1, 2, 3}, Ping Zhao¹

4 ¹State Key Laboratory of Severe Weather, Chinese Academy of Meteorological Sciences, Beijing, 100081, China

5 ²Collaborative Innovation Center on Forecast and Evaluation of Meteorological Disasters, Nanjing University of Information
6 Science and Technology, Nanjing 210044, China

7 ³Shandong Meteorological Service Center, Jinan, 250031, China

8 Correspondence to: Ping Zhao (zhaop@cma.gov.cn)

9 **Abstract** The important roles of the Tibetan Plateau (TP) atmospheric boundary layer (ABL) in climate, weather and air
10 quality have long been recognized, but little is known about the TP ABL climatological features and their west-east
11 discrepancies due to the scarce data in the western TP. Based on intensive sounding, surface sensible heat flux, solar
12 radiation, and soil moisture observational datasets from the Third Tibetan Plateau Atmospheric Scientific Experiment and
13 the routine meteorological operational sounding and ground-based cloud cover datasets in the Tibetan Plateau for the period
14 2013-2015, we firstly investigate the west-east differences in summer ABL features over the TP and the associated
15 influential factors. It is found that the heights of both the convective boundary layer (CBL) and the neutral boundary layer
16 (NBL) exhibit a diurnal variation and a west-east difference in the TP, while these features are not remarkable for the stable
17 boundary layer (SBL). Moreover, the ABL shows significant discrepancies in the amplitude of the diurnal variation and the
18 persistent time of the development between the eastern and western TP. In the early morning, the ABL height distribution is
19 narrow, with a mean height below 450 m above ground level (AGL) and a small west-east difference. The SBL observed at
20 this moment accounts for 85% of the TP total ABL. At noon, there are a wide distribution in the ABL height up to 4000 m
21 AGL and a large west-east difference of the ABL height, with a mean height above 2000 m AGL in the western TP and
22 around 1500 m AGL in the eastern TP. The CBL accounts for 77% of the TP total ABL at this moment, with more than 50%
23 of the CBL above 1900 m AGL. In the late afternoon, the CBL and SBL dominate the western and eastern TP, respectively,
24 which results in a larger west-east difference of 1054.2 m between the western and eastern TP. The high ABL height in a
25 cold environment over the western TP (relative to the plain areas) is similar to that in some extreme hot and arid areas such
26 as Dunhuang and Taklimakan Deserts. In general, for the western (eastern) TP, there is low (high) total cloud coverage, with
27 large (small) solar radiation at the surface and dry (wet) soil. These features lead to high (low) sensible heat flux and thus
28 promotes (inhibits) the local ABL development. This study provides new insights for west-east structures of the summer
29 ABL height, occurrence frequency, and diurnal amplitude over the TP region and the associated reasons.

30 **1 Introduction**

31 The atmospheric boundary layer (ABL) commonly refers to the bottom layer of the troposphere directly coupled with the
32 earth's surface at a response time scale of about one hour or less, in which a variety of complex motions characterized by
33 turbulence may be present (Stull, 1998). The turbulent motions in the ABL are responsible for the atmospheric mixing
34 processes, which affects the vertical redistribution of water vapour, momentum, heat, and atmospheric pollutants (Stull, 1988;
35 Garratt, 1992; Huang et al., 2007; Miao et al., 2015). The ABL height (ABLH) as a fundamental variable is critical to
36 diagnose turbulent mixing, vertical disturbance, convective transport, pollutant dispersion, and atmospheric environmental
37 and effective heat capacity (Garratt, 1993; Seibert et al., 2000; Guo et al., 2009; Esau and Zilitinkevich, 2010; Dai et al.,
38 2014; Palet et al., 2015; Davy and Esau, 2016). Therefore, the accurate specification of the ABLH is essential to develop
39 weather, climate, and air pollution prediction models.

40

41 The cloud-free ABL overland can be divided into three types, that is, the convective boundary layer (CBL), the stable
42 boundary layer (SBL), and the neutral boundary layer (NBL) (Stull, 1998). The CBL usually has the strongest turbulence
43 forced by surface buoyancy flux with or without wind shear, and is generally capped by a strong temperature inversion
44 maintained through large-scale subsidence. The CBL height is a result of the balance of the turbulence-induced entrainment
45 and the subsidence velocity (e.g. Driedonks and Tennekes, 1984). However, turbulence in the SBL is mainly driven by the
46 mean wind shear against negative buoyancy flux from the stable thermal stratification within the nocturnal surface inversion
47 (NSI). The SBL height is hence related to the boundary layer wind and wind shear, which sometimes are used to identify the
48 SBL height. The NBL occurs in neutral conditions with the turbulence of almost the same intensity in all directions (Stull,
49 1988; Blay-Carreras et al., 2014). It denotes the type of boundary layer with solely wind forcing and normally occurs during
50 the transition from the daytime CBL to the night time SBL. It can also occur anytime when the buoyancy forcing is weak.
51 The ABLH variability is dominated by its strong diurnal cycle (Stull, 1988; Garratt, 1992). In this diurnal cycle, the different
52 manifestations of an ABLH are generated in response to the distinct forcing mechanisms that originate from mechanical
53 (wind shear) and thermal (buoyancy) effects (Stull, 1988; Garratt, 1992). Over land and after sunrise, the surface is heated by
54 solar radiation, resulting in upward heat flux that initiates strong updrafts of warm air. Such a mechanism generates a
55 deepening of the CBL (Chen et al., 1997). At sunset, the surface cools more rapidly compared to the air above, resulting in
56 negative heat flux that consumes turbulent kinetic energy. Consequently, shear-driven turbulence can only maintain a
57 shallow SBL with the formation of the NSI (Zhang et al., 2011a; Miao et al., 2015). Above the NSI, the convective energy-
58 containing eddies start to lose their strength and mixing capacity. This deep and near-adiabatic vertical region, which is the
59 remnant of the daytime CBL, is known as the residual layer (RL). The use of precise information on the RL in numerical
60 models is of fundamental importance when describing the evolution of the diurnal CBL (Blay-Carreras et al., 2014; Chen et
61 al., 2016).

62

63 The ABLH can be calculated from temperature, humidity, and wind profiles (Holtslag and Boville, 1993; Seibert et al., 2000;
64 Seidel et al., 2010; Bosveld et al., 2014; Davy, 2018). The CBL height is generally less than 2000–3000 m AGL and the SBL
65 thickness is usually less than 400–500 m AGL (Garratt, 1992). The ABL height shows an obvious spatial variation due to
66 differences in topography, thermal properties of the underlying surface, and weather conditions. For example, the CBL can
67 grow to the height of 4700 m AGL in New Delhi before the outbreak of the South Asian monsoon, whereas it only reaches
68 900 m AGL in Bangalore during the monsoon period (Raman et al., 1990). Seidel et al. (2010, 2012) pointed out that a large
69 east-west spatial gradient of the ABLH at sunset in the United States spanning several time zones may be conflated with the
70 diurnal variations of the ABL for the local solar time in the west earlier than in the east at fixed observation times. Guo et al.
71 (2016) identified three large-scale ABLH spatial patterns in China, that is, a west-east gradient during sunrise, an east-west
72 gradient during sunset, and a south-north gradient at noon. The reasons for the first two patterns are similar to those in the
73 United States shown in Seidel et al. (2012), while the south-north gradient may be related to the local surface and
74 hydrological processes (Guo et al., 2016; Zhang et al., 2017).

75

76 The Tibetan Plateau (TP) with an average elevation exceeding 4000 m is characterized by complex land surface processes
77 and boundary layer structures (Tao and Ding, 1981; Yanai and Li, 1994; Xu et al., 2002; Yang et al., 2004; Li et al., 2007;
78 Sun et al., 2007; Zhao et al., 2018). The ABLH in the TP can reach 2000–3000 m AGL, generally higher compared to some
79 plains areas (with the ABLH of 1000–1500 m AGL) (Ye et al., 1979; Zhao et al., 1992; Xu et al., 2002; Zhang et al., 2003).
80 The ABLH in the TP varies greatly with location and season. At Gaize station of the western TP, the super-thick ABLH
81 may exceed 5000 m AGL during winter (Chen et al., 2013, 2016). In the central TP, the ABLH is lower, between 400 and
82 1800 m AGL at Dangxiong station and 1750 m AGL at Namucuo Lake (Li et al., 2000; Liu et al., 2001, and Lü et al., 2008).
83 Moreover, there is also a significant difference in the TP ABLH between dry and rainy seasons (Zuo et al., 2004). For
84 instance, the ABLH at Naqu station is 2211–4430 m AGL in the dry season, while it is 1006–2212 m AGL in the rainy
85 season (Li et al., 2011).

86

87 Although observations and studies for the TP ABL features have made progress, routine meteorological operational
88 sounding observations are scarce in the western TP due to the local high elevations, naturally harsh environmental conditions,
89 and logistic challenges. The previous studies on the ABL in the western TP are usually based on observational data at
90 Shiquanhe (during 15 days in one summer) and Gaize (during 22 days in one summer) stations (Song et al., 1984; Chen et al.,
91 2013). Thus, the statistical representation of their results is limited. Moreover, there are significant differences in surface
92 properties and general climate between the eastern and western TP (Wang et al., 2016). Few studies examined the west-east
93 differences in the ABL features due to the scarce data in the western TP. To obtain a longer observational data in the western
94 TP, the Third Tibetan Plateau Atmospheric Scientific Experiment (TIPEX-III) has made routine sounding launches at
95 Shiquanhe, Gaize, and Shenzha stations of the western TP (Fig. 1) since 2013, which fills in the data gaps in the operational
96 sounding network over the western TP (Zhao et al., 2018). Meanwhile, the TIPEX-III also carried out the intensive sounding

97 observations in the TP and adjacent stations at 14:00 Beijing Time (06:00 UTC) in June, July, and August (Zhao et al.,
98 2019b). Compared to the previous field experiments over the TP, the TIPEX-III has a wider and longer coverage of sounding
99 observations over the western TP, providing valuable observational data for studying the ABL features in the western TP and
100 the west-east differences of these features in the TP during summer.

101

102 This study utilizes the TIPEX-III sounding observational data to investigate the features of the ABLH in the TP and their
103 differences between the western and eastern TP during summer, and analyzes the major factors affecting the ABLH in the
104 TP. The remainder of this paper is organized as follows. Main features of data and methods are described in Section 2. In
105 Section 3, the characteristics of the ABLH in the eastern and western TP and their regional differences are analyzed in detail.
106 In Section 4, the major factors affecting the ABLH in the TP and the west-east differences are examined. Discussions and
107 conclusions are given in Section 5.

108 **2 Data and analysis methods**

109 **2.1 Observation data**

110 The TIPEX-III carried out the intensive routine meteorological sounding observations at Shiquanhe (SQH), Gaize (GZ), and
111 Shenza (SZ) stations of the western TP (marked by red dots in Fig. 1) since the 2013 summer (Zhao et al., 2018), which have
112 been applied in research on the vertical structure of the upper troposphere and lower stratosphere at Gaize station during the
113 rainy season and the effects of assimilating the intensive sounding data on downstream rainfall (Hong et al., 2016; Yu et al.,
114 2018; Zhao et al., 2018; Zhao et al., 2019b). These intensive sounding data and the routine meteorological operational
115 sounding data at 16 stations of the central-eastern TP from the China Meteorological Administration (marked by black dots
116 in Fig. 1) are utilized in this study. The sounding observations at the above intensive and operational sounding stations were
117 carried out at 08:00 Beijing Time (BJT; 00:00 UTC), 14:00 BJT (06:00 UTC), and 20:00 BJT (12:00 UTC) each day during
118 summer (June, July, and August), including vertical profiles of temperature, humidity, and wind direction and speed. After
119 the quality control of the sounding observational data, we select data from three time periods for this study: 15 June to 31
120 July 2013, 15 June to 31 August 2014, and 1 June to 31 August 2015. There are 11,635 sounding profiles (Fig. 1a) from 19
121 stations over the TP region consisting of 4745, 2049, and 4841 profiles at 08:00 BJT (Fig. 1b), 14:00 BJT (Fig. 1c), and
122 20:00 BJT (Fig. 1d), respectively. It is evident that the observational sample size used in this study is much more compared
123 to the previous studies. Meanwhile, it is noted that there is a large difference in the sample size between the intensive and
124 operational observation records at 08:00 BJT and 20:00 BJT (Fig. 1b and d), which is called the original dataset for
125 convenience. Consequently, we also select the test group dataset which contains the same intensive observation records as
126 the operational ones at these two times to make sensitivity analysis (shown in Section 3.2), which shows that the difference
127 in the sample size between the intensive and operational observation records does not change our conclusions.

128

129 To analyze the factors affecting the ABL in the TP, we use the TIPEX-III 30-min mean surface sensible heat flux (SHF),
130 downward solar radiation, and 5-cm soil volume moisture content at SQH (bare soil with less vegetation), Naqu (NQ; alpine
131 steppe), and Linzhi (LZ; alpine meadow with few shrubs and trees) stations in the 2014-2015 summers (Wang et al., 2016;
132 Zhao et al., 2018; Li et al., 2019, 2020). In addition, the manual operational ground-based cloud cover observations at 02:00,
133 08:00, 14:00, and 20:00 BJT from the China Meteorological Administration are also used in this study. These ground-based
134 could cover data have been utilized by Guo et al. (2016) and Zhang et al. (2017).

135

136 2.2 Calculation method of ABLH

137 The potential temperature gradient method, proposed by Liu and Liang (2010) and sketched in Fig. 2a, is utilized in
138 identifying the ABL type and calculating the ABL height. The CBL height is defined at the base of the overlying inversion
139 layer that caps the rising convective thermals. The SBL height is defined as the top of the underlying inversion layer, where
140 turbulence decreasing from the surface nearly ceases (Stull 1988). In the evening and morning transition periods when the
141 RL may occur, the neutral RL starting from the ground surface is identified with near-neutral conditions in the surface layer
142 (that is the NBL).

143

144 Following Liu and Liang (2010), Zhang et al. (2017), and Zhao et al. (2019a), the original sounding observation profiles with
145 a fine vertical resolution of ~ 1 hPa are interpolated to a vertical resolution of 5 hPa (corresponding to a vertical interval
146 around 50 m in the ABL) by the nearest neighbor interpolation method. On the basis of the near-surface thermal gradient,
147 such as a potential temperature (θ) difference (PTD) between the fifth layer (~ 250 m; θ_5) and the second layer (~ 50 m; θ_2),
148 the ABL is classified as follows.

$$149 PTD = \theta_5 - \theta_2 \begin{cases} < -\sigma, & \text{for CBL} \\ > +\sigma, & \text{for SBL.} \\ \text{else, for NBL} \end{cases} \quad (1)$$

150 Here σ is the stability threshold of the near-surface potential temperature stratification. Since the neutral stratification
151 condition ($\sigma = 0$) is rare in nature, consistent with Liu and Liang (2010), σ is set to 1.0 K. The threshold value of the NBL is
152 set to -1.0 to 1.0. Consequently, SBLs and CBLs with weak stable or unstable stratification are possibly identified as NBLs.

153

154 Once the boundary layer regime has been identified, we use the criteria defined by Liu and Liang (2010) to estimate the
155 ABLH for each regime. Since buoyancy is the dominant mechanism driving turbulence in the CBL, the ABLH is defined as
156 the height at which an air parcel rising adiabatically from the surface becomes neutrally buoyant (Stull 1988). First, we find
157 the lowest level (k_1) (Fig. 2a) that meets the following condition

$$158 \theta_{k_1} - \theta_1 \geq \sigma_u, \quad (2)$$

159 in which σ_u is the θ increment that represents the minimum strength of the unstable layer. Once level k_1 is determined,
 160 another upward scan is performed to find the lowest level at which the potential temperature gradient with height ($\dot{\theta}_k$) meets
 161 the following criteria
 162

$$\dot{\theta}_k \equiv \frac{\partial \theta_k}{\partial z} \geq \dot{\theta}_r. \quad (3)$$

163 Here $\dot{\theta}_r$ is the minimum strength for the overlying inversion layer and can be considered as the overshooting threshold of
 164 the rising parcel to define the scope of the entrainment zone for the CBL. The same procedure is adopted to determine the
 165 NBL height excluding the entrainment zone at the top (Fig. 2a). Various values of σ_u and $\dot{\theta}_r$ will affect the determination of
 166 the boundary layer height and they are respectively set to 0.5 K and 4.0 K km⁻¹, consistent with Liu and Liang (2010). For
 167 the SBL, the turbulence in the ABL can result from either buoyancy forcing or wind shear. The SBL height is defined as the
 168 lower of the heights of both the thermal stable layer from the surface and the maximum wind in the low-level jet stream if
 169 present. More details of the definitions of the boundary layer regimes may be seen in Liu and Liang (2010). Figure 2c-d
 170 shows the typical profiles of potential temperature for CBL, NBL, and SBL at 20:00 BJT on June 10, 2013, July 21, 2013,
 171 and August 11, 2013 at Lasa station, and the ABL heights calculated by the potential temperature gradient method are 3465,
 172 1258, and 409 m AGL, respectively.

173 **3 Characteristics of the summer ABLH in the eastern and western TP**

174 **3.1 A general characteristic of the ABLH**

175 The diurnal variation is an important feature of the ABL, consisting of different periods of daytime, night-time, and
 176 day/night transitions (Liu and Liang, 2010). In the central TP (near 90 °E), 08:00 BJT, 14:00 BJT, and 20:00 BJT correspond
 177 to 06:00 (the early morning), 12:00 (noon), and 18:00 (the late afternoon) local solar time (LST), respectively. To reveal a
 178 difference in ABLH between the eastern TP (ETP) and the western TP (WTP), we divide all sounding stations in the TP into
 179 two groups. One is for the WTP (to the west of 92.5 °E) with 8 stations, and the other is for the ETP (to the east of this
 180 longitude) with 11 stations.

181

182 Figure 3a-c shows the spatial distributions of the mean ABLH over the TP at 08:00 BJT, 14:00 BJT, and 20:00 BJT,
 183 respectively. In the early morning (08:00 BJT), the ABL is of the night-time property. The ABLH is generally low (<450 m
 184 AGL) over the TP and displays a relatively homogeneous feature (Fig. 3a). At this moment, the distribution of the ABLH is
 185 narrow, with a frequency peak of 35% at the ABLH of 300 m AGL (Fig. 3d) and 78.5% (99.6%) of the ABLH below 500
 186 (1000) m AGL (Fig. 3e). Figure 3f displays the zonal sections of the ABLH along 32 °N, in which the cross section includes
 187 SQH, GZ, SZ, NQ, CD, GanZ, and HY stations. In this figure, the ABLH varies between 218.4 and 433.9 m AGL from east
 188 to west and presents a relatively homogeneous feature in the west-east direction.

189

190 At noon (14:00 BJT), with the well developing of the daytime ABL (Fig. 3b), its height remarkably increases over the TP
191 with an average of 1887.7 m AGL and exhibits a large west-east difference. There is a wide distribution of the ABLH up to
192 4000 m AGL, with a relatively flat peak between 900 and 2900 m AGL (Fig. 3d) and only 17.8% (more than 50%) of the
193 ABLH below 1000 (above 1900) m AGL (Fig. 3e). At this moment, the regional mean ABLH is 2124.2 m AGL in the WTP
194 and 1693.5 m AGL in the ETP, with a mean difference of 430.7 m between the WTP and the ETP. Along 32°N, the ABLH
195 remarkably increases from 1379.4 m AGL at GanZ station to 2504.2 m AGL at SQH station, with the west-east difference
196 exceeding 1200 m (Fig. 3f). This regional difference in the TP ABLH could be likely related to the hydrologic factors such
197 as air moisture and soil water (also see Section 4) that may modulate the spatial distribution of the daytime ABLH (Seidel et
198 al., 2012).

199

200 In the late afternoon (20:00 BJT), the ABL begins to turn to the night-time feature. The ABLH also starts to decrease in the
201 ETP, with the regional mean height < 1000 m AGL, while it continues to increase at the west-most stations, with the regional
202 mean height > 2000 m AGL (Fig. 3c). This result indicates a larger west-east difference (1054.2 m) between the WTP and
203 the ETP. Especially, the ABLH is 602 m AGL at HY station and 2920.6 m AGL at SQH station, with a difference above
204 2000 m between these two stations (Fig. 3f). At this moment, the frequency of the high ABLH decreases, with 12.8% of the
205 frequency peak at the ABLH of 300 m AGL (Fig. 3d) and 50% of the ABL heights less than 1000 m AGL (Fig. 3e). It is
206 evident that the west-east difference of the ABLH over the TP increases from noon to the late afternoon. After sunset, the
207 daytime boundary layer undergoes a transition to the night-time boundary layer. Since the TP spans almost 1.5 time zones
208 from west to east (15° longitudes equals 1 hour time difference), the local solar time is earlier in the west compared to the east,
209 which supports an earlier transition from the daytime ABL to the night-time ABL in the east (Seidel et al., 2010, 2012; Guo
210 et al., 2016).

211

212 Figure 4 further shows the variations of the ABLH from 08:00 BJT to 14:00 BJT and from 14:00 BJT to 20:00 BJT,
213 indicating varying rates in 6 h. It is seen from Fig. 4a that the ABLH in the TP increases substantially from 08:00 to 14:00
214 BJT, with a mean growth rate of 1500 m/6 h. There is also a large west-east difference of the ABLH growth rate in this
215 period, with the regional mean of 1800 m/6 h and 1300 m/6 h in the WTP and the ETP, respectively. From 14:00 to 20:00
216 BJT (Fig. 4b), the growth rate of the ABLH is negative in the ETP, exhibiting an opposite trend to that in Fig. 4a, which
217 indicates a significant decrease (around -600 m/6 h) of the ABLH after noon. In the WTP, the growth rate generally shows a
218 weak increase (around 400 m /6 h) or decrease (around -140 m /6 h). It is evident that the growth rate from 08:00 to 14:00
219 BJT may indicate the amplitude of the ABL diurnal variation over the TP. Compared to the ETP, the ABL in the WTP has
220 the larger amplitude of the diurnal variation and the longer development time.

221

222 **3.2 Characteristics of SBL, NBL, and CBL heights**

223 We further examine the characteristics of different ABL types. Figure 5 presents the spatial distribution of occurrence
224 frequency of SBL, NBL and CBL at 08:00 BJT, 14:00 BJT, and 20:00 BJT. It is seen that the occurrence frequency exhibits
225 significant discrepancies at different times for the SBL and CBL. At 08:00 BJT, the occurrence frequency of the SBL/CBL is
226 large/little (Fig. 5a/Fig. 5g), with a mean value 84.9%/8.5% over the TP. At 14:00 BJT, the occurrence of the SBL/CBL
227 remarkably decreases/increases, accounting for 3.1%/76.9% of the ABL (Fig. 5b/Fig. 5h). At 20:00 BJT, the SBL/CBL
228 mainly occurs in the ETP/WTP (Fig. 5c/Fig. 5i), with a regional mean of 35.0%/65.0%. However, the NBL shows a
229 relatively weaker temporal variation over the TP (Fig. 5d-f), with the mean occurrence frequency of 6.4%, 20.0%, and 25.5%
230 at 08:00 BJT, 14:00 BJT, and 20:00 BJT, respectively. The above results are consistent with the diurnal development of the
231 ABL structure including the SBL in the early morning, the CBL at noon, and different types of ABLs between the eastern
232 and western TP in the late afternoon because of the latitudinal difference and the resultant difference in local solar times.
233 Note that the observations were made simultaneously for all stations. Nevertheless, the daytime SBL and the night-time CBL
234 may also occur with low frequencies in the TP, which is likely due to the ‘abnormal’ forcing associated with certain synoptic
235 conditions or cloud coverage (Medeiros et al., 2005; Poulos et al., 2002; Stull, 1988).

236

237 To analyse the temporal variations of the ABLH over the TP, the ABL height-occurrence frequency relationships for the
238 SBL, NBL, and CBL at 08:00 BJT, 14:00 BJT, and 20:00 BJT are presented in Fig. 6a-f. For the SBL, the frequency
239 distribution of the ABLH shows the similar feature at three measurement times (Fig. 6a-c) and is characterized by a narrow
240 single mode, with the frequency peaks of 39.0%, 28.1%, and 36.6% at the ABLH of 200, 300, and 300 m AGL at 08:00,
241 14:00, and 20:00 BJT, respectively, which indicates small temporal variations of the SBL height due to its turbulence
242 inhabited. Moreover, the SBL height above 80% is < 600 m AGL and the cumulative frequency of the SBL height exceeding
243 1000 m AGL is little (near zero) at 08:00, 14:00, and 20:00 BJT (Fig. 6d, e, and f). For the NBL and CBL, however, their
244 heights vary strongly with time under the influence of surface heating in the daytime. At 08:00 BJT (Fig. 6a), the
245 distributions of the NBL and CBL heights are narrow, with the frequency peaks of 27.5% and 35.1% at the ABLH of 300 m
246 AGL for NBL and CBL, respectively, similar to that of the SBL, which is possibly due to the initial development of the CBL
247 and NBL in the early morning. At 14:00 BJT, the CBL and NBL have a wide distribution of the ABLH up to 4000 m AGL,
248 with a relatively flat peak between 1000 and 3000 m AGL, which is remarkably different from a single peak of the SBL. The
249 frequency of the NBL height between 500 and 3000 m AGL is generally less than 5% (Fig. 6b), with a frequency peak of 6.1%
250 at 1000 m AGL, and more than 50% NBL height exceeds 1700 m AGL (Fig. 6e). The height of the CBL is higher, with a
251 frequency peak near 4.5% between 1500 and 2500 m AGL (Fig. 6b) and more than 50% CBL height is above 2000 m AGL
252 (Fig. 6e). These results show that the ABL develops well at noon. When the ABL begins turning to the night-time property at
253 20:00 BJT (Fig. 6c and 6f), the distributions of the CBL and NBL heights are still wide but the frequency of the high ABL
254 height decreases, with the frequency peak below 500 m AGL. It is obvious that the CBL and NBL heights show the similar

255 results consistent with those from Zhang et al (2017). Stull (1998) and Blay-Carreras et al. (2014) revealed that the NBL
256 often occurs in the transition periods between the CBL and the SBL. Since these transitions occur rapidly, the NBL may
257 have the same characteristics in the state variables as the CBL prior to the transition although the dynamic forcing in the
258 NBL maybe weaker compared to the CBL.

259

260 To reveal the spatial variations of the ABLH over the TP, the distributions of mean SBL, NBL, and CBL heights at 08:00
261 BJT, 14:00 BJT, and 20:00 BJT are illustrated in Fig. 7. The SBL height is generally low and varies between 200 and 730 m
262 AGL at these times, with a mean height of 336.0 m AGL at 08:00 BJT, 356.0 m AGL at 14:00 BJT, and 321.9 m AGL at
263 20:00 BJT (Fig. 7a-c), which indicates the weak spatial differences of the SBL height over the TP at three observation times.
264 For the NBL and CBL, their heights are still low in the early morning (Fig. 7d and 7g), with the ABLH < 450 m AGL, and
265 have small spatial differences. At noon (Fig. 7e and 7h), the NBL and CBL heights rapidly increase, especially in the WTP,
266 which leads to a remarkable east-west gradient in the ABL height. At this moment, there is a regional mean NBL/CBL
267 height of 2074.6/2191.4 m AGL in the WTP and 1594.8/1788.0 m AGL in the ETP, with a difference of 479.8/403.4 m
268 between the WTP and the ETP. In the late afternoon (Fig. 7f and 7i), the NBL/CBL height continues to increase in the WTP,
269 with a regional mean of 2092.0/2192.2 m AGL, while the NBL/CBL height begins decreasing in the ETP, with a regional
270 mean of 1423.1/1237.2 m AGL. This varying feature in the ETP and WTP results in the larger differences of 668.9/955.0 m
271 in the NBL/CBL height between the WTP and ETP. Thus there is a significant difference in the frequency distribution of the
272 ABL height between the ETP and the WTP in the daytime (Fig. 6g). The cumulative frequency contours gradually go
273 upward from east to west (Fig. 6h). The eastern TP is dominated by a low CBL height, with the peak of 14.4% at the height
274 of 350 m AGL (Fig. 6g) and the 50% (5%) CBL height below 1000 m AGL (above 2500 m AGL) (Fig. 6h). For the WTP,
275 the strong peak of 4%-10% corresponds to the high CBL between 2500 and 3500 m AGL (Fig. 6g), especially at SQH
276 station, and there are larger CBL heights, with almost 50% CBL extending upward to more than 2500 m AGL, almost 10%
277 reaching 4000 m AGL or higher, and only 15% CBL below 1000 m AGL (Fig. 6h).

278

279 To investigate an effect of differences in the sample profiles shown in Fig. 1b and d, we use the test group dataset to repeat
280 the above analyses. Figures 8a and b show the scatter plots of the occurrence frequency of the SBL, NBL, and CBL from the
281 original and test group datasets at each of 19 stations at 08:00 BJT and 20:00 BJT, respectively. It is seen that the correlation
282 coefficients between the two datasets are 0.92-0.99, with root-mean-square errors (RMSEs) of the occurrence frequency
283 between 1.1% and 2.7%. The similar results are also seen in the SBL, NBL, and CBL heights at 08:00 BJT (Fig. 8c) and
284 20:00 BJT (Fig. 8d). The correlation coefficients in the ABL height are 0.90-0.99. The RMSE of the SBL height is 14 m and
285 25 m at 08:00 and 20:00 BJT, respectively. The RMSE of the CBL and NBL heights are 54-59 m at 08:00 BJT and 99-107m
286 at 20:00 BJT. These high correlations and little errors show that the difference in the sample size does not change our
287 conclusions.

288

289 From the foregoing analysis, the CBL and NBL heights in the TP show remarkable temporal variations and west-east spatial
290 differences, while these features are not remarkable for the SBL. From noon to the late afternoon, the NBL and CBL are
291 deeper in the WTP compared to the ETP, with the ABLH difference between the WTP and the ETP exceeding 600 m AGL
292 at 20:00 BJT. Then, which factors contribute to this difference in the ABL between the WTP and ETP? In the following
293 section, we examine some factors that may be responsible for the ABL height over the TP.

294 **4 Factors responsible for the ABL height over the TP**

295 Previous studies have addressed effects of surface sensible heat flux (SHF), soil volume moisture content (VWC), downward
296 solar radiation flux (DSR), and the cloud cover (CLD) on ABL height (Lilly, 1964; Liu, et al., 2004; Brooks and Rogers,
297 2006; Zhao et al., 2011; Sanchez-Mejia and Papuga, 2014; Rihani et al., 2015; Lin et al., 2016; Zhang et al., 2017; Zhang et
298 al., 2019; Qiao et al., 2019). However, these studies paid little attention to reasons for the west-east difference of the ABL
299 between the eastern and western TP. To investigate a possible reason for this difference, we utilize the TIPEX-III SHF, DSR,
300 and VWC at SQH, NQ, and LZ stations, and the corresponding meteorological operational CLD observations to analyze the
301 relationships between these variables and the ABL height.

302
303 The driving force of turbulence in the ABL is the surface buoyancy flux as a result of surface and air temperature and
304 humidity differences and the mean surface layer wind. The kinematic heat flux (KHF) and kinematic moisture flux (KMF) at
305 the surface are the two directly factors responsible for the surface buoyancy flux (Brooks and Rogers, 2006). Since KMF is
306 often small, KHF associated with SHF is examined as a major component of buoyancy flux in dry conditions over land.
307 According to the method of Brooks and Rogers (2006), our calculation results show that the contribution from KMF to
308 surface buoyancy flux is below 18% at SQH, NQ, and LZ stations. Moreover, the ABL may be largely affected by the effect
309 of cumulative SHF in the daytime (Zhang et al., 2019). Thus we analyse the possible effect of SHF on the ABL. Figure 9a-c
310 presents the scatter plots between the mean SHF over the past six hours and the ABL height at SQH, NQ, and LZ stations.
311 As shown in this figure, the correlation is 0.80, 0.81, and 0.71 (significant at the 99% confidence level) at these stations,
312 respectively. When SHF is strong, the turbulent motion is strong and the ABL develops, which is consistent with the result
313 of Zhang et al. (2011b). Their result shows a significant correlation of 0.78 in the arid area of Northwest China between the
314 ABL thickness and the cumulative SHF. Figures 10a and b further present the features of the ABL height and SHF at SQH,
315 NQ, and LZ stations. The mean value of SHF is 85 W/m², 42 W/m², and 33 W/m² at SQH, NQ and GZ stations, respectively,
316 and has a large difference (52 W/m²) between SQH and NQ stations. This result indicates a decreasing trend of SHF from
317 west to east in the TP, consistent with a reduction of the ABL height from SQH via NQ to LZ station (shown in Figs. 3 and
318 10a). In addition, Fig. 11 demonstrates the diurnal variations of SHF and the ABL height at SQH, NQ, and LZ stations. The
319 duration of positive SHF in a diurnal cycle at SQH, NQ and GZ stations is 14, 12 and 11 hours, respectively, and indicates a
320 decreasing trend from west to east in the TP. It is clear that the peak of the SHF occurs earlier than the maximum ABLH in a

321 diurnal cycle at SQH station. The maximum ABL height occurs near 20:00 BJT (approximately 17:20 LST), corresponding
322 to a strong SHF. At LZ station, however, the SHF turns into a negative value at 20:00 BJT (18:20 LST) and then the ABL
323 height decreases. Some past studies show that the development of ABL height generally lags the development of SHF, and
324 ABL depth growth continues even after SHF attains the maximum daytime value until the time of early evening transitions
325 (Chen et al., 2016; Zhang et al., 2019). Consequently, the difference in the ABL height between the WTP and ETP is closely
326 associated with a west-east difference in SHF that is as a direct thermal factor for the ABL development in the TP.
327

328 The solar radiation at the surface is an important component of the surface energy budget, affecting surface temperature and
329 SHF. We show the scatter plots between the 6-hour mean DSR and the ABL height at SQH, NQ, and LZ stations (Fig. 9d-f).
330 The ABL height is highly correlated with the 6-hour average of DSR at these stations, with the correlation coefficients of
331 0.86, 0.81, and 0.73, respectively, which is equivalent to those of SHF. The mean DSR shows a decreasing trend from SQH
332 (510 W/m^2) to LZ (200 W/m^2) station. Since the solar irradiance at the surface is negatively associated with the local cloud
333 cover (Guo et al., 2011; Lin et al., 2016; Li et al., 2017; Zhang et al., 2017), the cloud cover is also correlated to the ABL
334 height. Figure 9g-i shows that the 6-hour mean CLD has significant correlations of -0.56, -0.65, and -0.54 with the ABL
335 height at SQH, NQ, and LZ stations, respectively. A decrease of the mean ABL height from SQH to LZ station (Fig. 10a) is
336 corresponded to an increase of cloud cover (Fig. 10d) and a decrease of DSR (Fig. 10c). When cloud cover is between 0 and
337 20%, the mean ABL height for the NBL and CBL is 2019 m AGL/2732 m AGL in the ETP/WTP; and when cloud cover
338 is >80%, the ABL height decreases to 741 m AGL/1626 m AGL in the ETP/WTP (Fig. 12). Therefore, the increased cloud
339 cover inhibits the development of both the NBL and CBL. The difference in cloud cover between the WTP and ETP
340 contributes to the west-east distribution of DSR and SHF, also finally contributing to the difference of the ABL development.
341 Corresponding to more cloud cover in the ETP, the local ABL is more closely associated with atmospheric moisture
342 processes.

343
344 Soil moisture is also an important factor affecting SHF. Low soil moisture generally coincides with a high surface sensible
345 heat flux, which facilitates the ABL development (e.g., McCumber and Pielke, 1981; Sanchez-Mejia and Papuga, 2014;
346 Rihani et al., 2015). Figure 9j-l shows that the relationship between the ABL height and the 6-hour mean VWC at SQH, NQ,
347 and LZ stations. The ABL height at LZ station is negatively correlated to the local soil moisture, with a significant
348 correlation coefficient of -0.45. This result indicates that the ABL height is lower when surface soil is moister. However, the
349 negative correlation is weaker at SQH station, with a correlation coefficient of -0.21. This difference between the WTP and
350 the ETP may be associated with the climatic feature of the local soil moisture. The surface type transitions from alpine
351 meadow with few shrubs and trees or alpine steppe in the ETP to bare soil with few obstacles in the WTP (Lin et al., 1981;
352 Wang et al., 2016). Accordingly, soil moisture decreases gradually from the ETP to the WTP (Fig. 10e), with a mean value
353 of soil moisture below $0.10 \text{ m}^3/\text{m}^3$ at SQH station and $0.38 \text{ m}^3/\text{m}^3$ at LZ station. Little soil moisture in the WTP has a weak

354 modulation to the local surface heat flux, which may lead to a weak correlation between the ABL height and soil moisture in
355 the WTP.

356 **5 Summary and discussion**

357 Using the summer TIPEX-III intensive and meteorological operational observational datasets, we examine the ABL features
358 and the relationships of the ABL height with surface sensible heat flux, solar radiation, cloud cover, and soil moisture in the
359 TP region. The main conclusions are summarized as follows.

360

361 Generally speaking, the ABL height exhibits diurnal variations and regional differences in the TP, especially for the CBL
362 and NBL. These features are weak for the SBL. Compared to the ETP, the ABL in the WTP has the larger amplitude of the
363 diurnal variation and the longer development time. In the early morning, the ABL height is generally low over the TP, not
364 showing a large west-east difference, and the distribution of the ABL height is narrow, with 78.5% of the ABL height < 500
365 m AGL. At noon, the CBL and NBL heights remarkably increase and have a wide distribution in the ABL height up to 4000
366 m AGL, with more than 50% of the ABL height exceeding 1900 m AGL. Their heights exhibit a large west-east difference.
367 At this moment, the distribution of the SBL height is also narrow, with the cumulative frequency of 80% at the height of 500
368 m AGL, and there is no remarkable west-east difference. In the late afternoon, there are a narrow distribution of the SBL
369 height and wide distributions of both the NBL and CBL heights. At this moment, the ABL height continues to increase in the
370 WTP, while it begins to decrease in the ETP. This feature results in a larger west-east difference in the ABL height. In spite
371 of a cold environment in the TP (relative to plain areas), the WTP still has the ABL height above 2000 m AGL, which is
372 similar to some extreme hot and arid areas such as Dunhuang and Taklimakan Deserts. In the ETP, the ABLH is similar to
373 that in North China (1500-1900 m AGL) and is generally larger compared to the East Asian summer monsoon region (<
374 1500 m AGL) such as the Yangtze River Delta and the Pearl River Delta (Zhang et al., 2011; Guo et al., 2016; Zhang et al.,
375 2017; Qiao et al., 2019).

376

377 The occurrence frequency of the SBL and CBL in the TP shows remarkable temporal variations. Most (few) of the SBLs
378 (CBLs) occur in the early morning and the occurrence frequency rapidly decreases (increases) at noon, accounting for 3.6%
379 (76.9%) of the ABL in the TP. Possibly owing to a difference in the solar elevation angle with respect to longitude in the late
380 afternoon, the SBL and CBL dominate the ETP and WTP, respectively. However, the NBL shows a relatively weak temporal
381 variation over the TP, with the mean occurrence frequency of 6.4% in the early morning and around 20% at noon and in the
382 late afternoon.

383

384 The ABL height is significantly correlated to SHF, DSR, and cloud cover in the TP and is also closely associated with soil
385 moisture in the ETP. The decreasing trends in both SHF and DSR and the increasing trends in both cloud cover and soil

386 moisture from west to east may cause the corresponding west-east reduction in the ABL height. In the WTP (ETP), with low
387 (high) cloud cover, there is larger (smaller) downward solar radiation at the surface. Meanwhile, corresponding to bare soil
388 (alpine meadow or steppe) in the WTP (ETP), there is a dry (wet) soil condition. These features cause high (low) sensible
389 heat flux, thus promoting (inhibiting) the local ABL development. The above factors affecting the WET and ETP ABL
390 heights are summarized in Fig. 13.

391

392 The Tibetan Plateau is an area very sensitive to global climate change, which exerts important thermal and dynamical effects
393 on the general circulation and climate through the unique and complex land surface and boundary layer processes. Owing to
394 new sounding observations in the WTP, our analysis firstly reveals remarkable west-east differences in the ABL height,
395 occurrence frequency, and diurnal amplitude over the TP region during summer. It is noted that there is a big drop in the
396 CBL height from 3000–4000 m AGL to 1000–2000 m AGL from the WTP to the ETP. Such a steep west-east
397 inhomogeneity in the TP (with an East-West spatial scale of about 2000 km) is remarkably different from the regional
398 variability of the ABLH on much larger scales (~4000 km) such as in the United States (Seidel et al., 2012) and in China
399 (Guo et al., 2016). This unique inhomogeneity in the TP may trigger the local mesoscale circulation and precipitation (Segal
400 et al., 1992; Goutorbe et al., 1997; Huang et al., 2009; Zhang et al., 2019; Qiao et al., 2019). Therefore, the influences of the
401 west-east differences in the ABLH over the TP on the local weather and climate should be further studied in the future. In
402 addition, this study merely investigates the characteristics of the summer ABLH in TP due to the limitation of the intensive
403 sounding observations. More efforts should be made to expand the climatology of ABLH to other seasons in TP when more
404 sounding data are available.

405

406 Code and data availability. All data used are available from the TIPEX-III on its homepages (<http://data.cma.cn/tipex>).

407

408 Author contributions. J.C. designed the study, analyzed the data and wrote the manuscript. P.Z. contributed to the study
409 design, supervisor, and writing of the manuscript.

410

411 Competing interests. The authors declare that they have no conflict of interest.

412

413 Acknowledgements. We thank the TIPEX-III for providing the data available on its homepages (<http://data.cma.cn/tipex>).
414 This work is supported by the National Key Research and Development Program of China and the Strategic Priority
415 Research Program of Chinese Academy of Sciences.

416

417 Financial support. This work is jointly funded by the National Key Research and Development Program of China (Grant
418 2018YFC1505700) and the Strategic Priority Research Program of Chinese Academy of Sciences (XDA20100300).

419 **References**

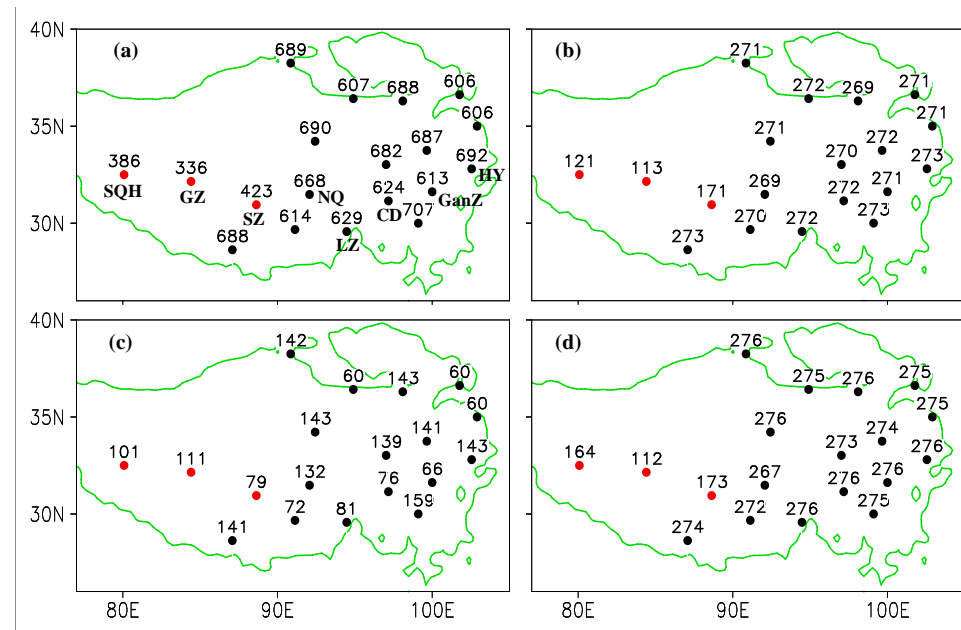
- 420 Blay-Carreras, E., Pino, D., Vil à-Guerau de Arellano, J., van de Boer, A., De Coster, O., Darbieu, C., Hartogensis, O., Lohou,
421 F., Lothon, M., Pietersen, H.: Role of the residual layer and large-scale subsidence on the development and evolution of the
422 convective boundary layer, *Atmos. Chem. Phys.*, 14, 4515–4530, doi:10.5194/acp-14-4515-2014, 2014.
- 423 Bosveld, F. C., and Coauthors: The third GABLIS intercomparison case for evaluation studies of boundary-layer models. Part
424 B: Results and process understanding, *Bound.-Layer Meteor.*, 152, 157–187, doi:10.1007/s10546-014-9919-1, 2014.
- 425 Brooks, I. M., Rogers, D. P.: Aircraft observations of the mean and turbulent structure of a shallow boundary layer over the
426 Persian Gulf, *Bound.-Layer Meteor.*, 95, 189–210, doi:10.1023/A:1002623712237, 2000.
- 427 Chen, S. S., and Houze, R. A.: Diurnal variation and life-cycle of deep convective systems over the tropical Pacific warm
428 pool, *Quart. J. Roy. Meteor. Soc.*, 123, 357–388, doi:10.1002/qj.49712353806, 1997.
- 429 Chen, X. L., Juan, A. Añel., Su, Z. B., Laura, de. La. Torre., Hennie, Kelder., Jacob, van. Peet., Ma, Y. M.: The deep
430 atmospheric boundary layer and its significance to the stratosphere and troposphere exchange over the Tibetan Plateau, *PLoS.*
431 ONE, 8, e56909, doi:10.1371/journal.pone.0056909, 2013.
- 432 Chen, X. L., Škerlak, B., Rotach, M. W., Juan, A. Anel., Su, Z. B., Ma, Y. M., Li, M. S.: Reasons for the extremely high-
433 ranging planetary boundary layer over the Western Tibetan Plateau in winter, *J. Atmos. Sci.*, 73, 2021–2038, doi:10.1175/jas-
434 d-15-0148.1, 2016.
- 435 Dai, C., Wang, Q., Kalogiros, J. A., Lenschow, D. H., Gao, Z., Zhou, M.: Determining boundary-layer height from aircraft
436 measurements, *Bound.-Layer Meteor.*, 152, 277–302, doi:10.1007/s10546-014-9929-z, 2014.
- 437 Davy, R., and Esau, I.: Differences in the efficacy of climate forcings explained by variations in atmospheric boundary layer
438 depth, *Nat. Commun.*, 7, 11690, doi:10.1038/ncomms11690, 2016.
- 439 Davy, R.: The climatology of the atmospheric boundary layer in contemporary global climate models, *J. Climate*,
440 doi:10.1175/JCLI-D-17-0498.1, 2018.
- 441 Driedonks, A. G. M. and Tennekes, H.: Entrainment effects in the well-mixed atmospheric boundary layer, *Bound.-Layer
442 Meteor.*, 30, 75–105, doi:10.1007/BF00121950, 1984.
- 443 Esau, I., and Zilitinkevich, S.: On the role of the planetary boundary layer depth in the climate system, *Adv. Sci. Res.*, 4, 63–
444 69, doi:10.5194/asr-4-63-2010, 2010.
- 445 Garratt, J. R.: The Atmospheric Boundary Layer, Cambridge, Univ. Press., 37, 89–134, doi:10.1007/3-211-38078-7_4, 1992.
- 446 Garratt, J. R.: Sensitivity of climate simulations to land-surface and atmospheric boundary-layer treatments—A review, *J.
447 Climate*, 6, 419–448, doi:10.1175/1520-0442(1993)006<0419:socstl>2.0.co;2, 1993.
- 448 Goutorbe, J. P., Lebel, T., Dolman, A. J., Gash, J. H. C., Kabat, P., Kerr, Y. H., Monteny, B., Prince, S. D., Stricker, J. N. M.,
449 Tinga, A., Wallace, J. S.: An overview of HAPEX-Sahel: A study in climate and desertification, *J. Hydrol.*, 188–189, 4–17,
450 doi:10.1016/S0022-1694(96)03308-2, 1997.

- 451 Guo, J. P., Zhang, X. Y., Che, H. Z., Gong, S. L., An, X., Cao, C. X.: Correlation between PM concentrations and aerosol
452 optical depth in eastern China, *Atmos. Environ.*, 43, 5876-5886, doi:10.1016/j.atmosenv.2009.08. 026, 2009.
- 453 Guo, J. P., Miao, Y. C., Zhang, Y., Liu, H., Li, Z. Q., Zhang, W. C., He, J., Lou, M. Y., Yan, Y., Bian, L. G., Zhai, P. M.:
454 The climatology of planetary boundary layer height in China derived from radiosonde and reanalysis data, *Atmos. Chem.
455 Phys.*, 16, 13309-13319, doi:10.5194/acp-16-13309-2016, 2016.
- 456 Holtslag, B. and Boville, B. A.: Local versus nonlocal boundary-layer diffusion in a global climate model. *J. Climate*, 6,
457 1825–1842, doi:10.1175/1520-0442(1993)0062.0.CO;2,1993.
- 458 Hong, J., Guo, J., Du, J., Wang, P.: An observational study on the vertical structure of the upper troposphere and lower
459 stratosphere in Gaize, Tibet during the rainy season, *Acta Meteor. Sinica*, 74, 827-836, doi:10.11676/qxxb2016.05, 2016.
- 460 Huang, J. P., Minnis, P., Yi, Y., Tang, Q., Wang, X., Hu, Y., Liu, Z., Ayers, K., Trepte, C., Winker, D.: Summer dust
461 aerosols detected from CALIPSO over the Tibetan Plateau, *Geophys. Res. Lett.*, 34, L18805, doi:10.1029/2007GL029938,
462 2007.
- 463 Huang, Q., Marsham, J. H., Parker, D. J., Tian, W., Weckwerth, T.: A comparision of roll and nonroll convection and the
464 subsequent deepening moist convection: An LEM case study based on SCMS data, *Mon. Wea. Rev.*, 137, 350-365,
465 doi:10.1175/2008MWR2450.1, 2009.
- 466 Li, J. L., Hong, Z. X., Sun, S. F.: An observational experiment on the atmospheric boundary layer in Gerze area of the
467 Tibetan Plateau, *Chinese J. Atmos. Sci.*, 24, 301-312, doi:10.3878/j.issn.1006-9895.2000.03.02, 2000.
- 468 Li, Y., Gao, W.: Atmospheric boundary layer circulation on the eastern edge of the Tibetan Plateau, China, in summer, *Arct.
469 Antarct. Alp. Res.*, 39, 708-713, doi:10.1657/1523-0430(07-50 4)[li]2.0.co;2, 2007.
- 470 Li, M. S., Ma, Y. M., Ma, W. Q., Ishikawa, Hirohiko., Sun, F. L., Ogino, S. Y.: Structural difference of atmospheric
471 boundary layer between dry and rainy seasons over the central Tibetan Plateau, *Journal of Glaciology and Geocryology*, 33,
472 72-79, doi:10.3724/SP.J.1146.2006.01085, 2011.
- 473 Li, Z., Guo, J., Ding, A., Liao, H., Liu, J., Sun, Y.: Aerosol and boundary-layer interactions and impact on air quality, *Natl.
474 Sci. Rev.*, 4, 810-833, doi:10.1093/nsr/nwx117, 2017.
- 475 Li, N., Zhao, P., Wang, J., Deng, Y.: Estimation of surface heat fluxes over the central Tibetan Plateau using the maximum
476 entropy production model, *J. Geophys. Res.-Atmos.*, 124, 6827–6840, doi:10.1029/2018JD029959, 2019.
- 477 Li, N., Zhao, P., Wang, J., Deng, Y.: The Long-Term Change of Latent Heat Flux over the Western Tibetan Plateau.
478 *Atmosphere*, 11, 262, doi:10.3390/atmos11030262, 2020.
- 479 Lin, Y., Wang, Y., Zhang, R., Liu, Y.: Response of boundary layer clouds to continental pollution during the RACORO
480 campaign, *J. Atmos. Sci.*, 73, 3681–3700, doi:10.1175/JAS-D-15-0361.1, 2016.
- 481 Liu, S. H., Xu, Y., Hu, F.: Using a Modified Soil-Plant-Atmosphere Scheme (MSPAS) to simulate the interaction between
482 land surface processes and atmospheric boundary layer in semi-arid regions, *Adv. Atmos. Sci.*, 21(2): 245-259,
483 doi:10.1007/bf029157 11, 2004.

- 484 Liu, S. Y., Liang, X. Z.: Observed diurnal cycle climatology of planetary boundary layer height, *J. Climate*, 23, 5790-5809,
485 doi:10.1175/2010JCLI3552.1, 2010.
- 486 Liu, H. Y., Miao, M. Q.: Preliminary analysis on characteristics of boundary layer in Qinghai-Tibet Plateau, *Journal of*
487 *Nanjing University (Natural Sciences)*, 37, 348-357, doi:10.3321/j.issn:0469-5097.2001.03.013, 2001.
- 488 Lü, Y. Q., Ma, Y. M., Li, M. S., Sun, F. L.: Study on characteristic of atmospheric boundary layer over Lake Namco region,
489 *Tibetan Plateau, Plateau Meteor.*, 27, 1205-1210, doi:ir.casnw.net/handle/362004/9294, 2008.
- 490 McCumber, M. C., and Pielke, R. A.: Simulation of the effects of surface fluxes of heat and moisture in a mesoscale
491 numerical model: 1. Soil layer, *J. Geophys. Res.*, 86, 9929-9938, doi:10.1029/JC086iC10p09929, 1981.
- 492 Miao, Y. C., Hu, X. M., Liu, S. H., Qian, T. T., Xue, M., Zheng, Y. J., Wang, S.: Seasonal variation of local atmospheric
493 circulations and boundary layer structure in the Beijing-Tianjin-Hebei region and implications for air quality, *J. Adv. Model.*
494 *Earth Syst.*, 7, 1602-1626, doi:10.1002/2015MS000 522, 2015.
- 495 Pal, S., and Haefelin, M.: Forcing mechanisms governing diurnal, seasonal, and interannual variability in the boundary layer
496 depths: Five years of continuous lidar observations over a suburban site near Paris, *J. Geophys. Res. Atmos.*, 120, 11936-
497 11956, doi: 10.1002/2015JD023268, 2015.
- 498 Qiao, L., Zhang, Q., Yue, P., et al.: Analysis of changes in the structure of atmospheric boundary layer from non-monsoon
499 zone to monsoon zone, *Chinese J. Atmos. Sci.*, 43 (2): 251-265, doi:10.3878/j.issn.1006-9895.1805.17231, 2019.
- 500 Raman, S., Templeman, B., Templeman, S., Holt, T., Murthy, A. B., Singh, M. P., Agarwaal, P., Nigam, S., Prabhu, A.,
501 Ameenullah, S.: Structure of the Indian southwesterly pre-monsoon and monsoon boundary layers: Observations and
502 numerical simulation, *Atmos. Environ.*, 24, 723-734, doi:10.1016/0960-1686(90)90273-p, 1990.
- 503 Rihani, J. F., Chow, F. K., Maxwell, R. M.: Isolating effects of terrain and soil moisture heterogeneity on the atmospheric
504 boundary layer: Idealized simulations to diagnose land atmosphere feedbacks, *J. Adv. Model. Earth Syst.*, 7, 915-937,
505 doi:10.1002/2014MS000371, 2015.
- 506 Sanchez-Mejia, Z. M., and Papug, S. A.: Observations of a two-layer soil moisture influence on surface energy dynamics
507 and planetary boundary layer characteristics in a semiarid shrubland, *Water Resour. Res.*, 50, 306-317, doi:10.1002/2013
508 WR014135, 2014.
- 509 Segal, M., Arritt, R. W.: Nonclassical mesoscale circulations caused by surface sensible heat-flux gradients, *Bull. Amer.*
510 *Meteor. Soc.*, 73, 1593-1604, doi:10.1175/1520-0477(1992)0732.0.CO;2, 1992.
- 511 Seibert, P., Beyrich, F., Gryning, S. E., Joffre, S., Rasmussen, A., Tercier, P.: Review and intercomparison of operational
512 methods for the determination of the mixing height, *Atmos. Environ.*, 34, 1001-1027, doi:10.1016/s1352-2310(99)00349-0,
513 2000.
- 514 Seidel, D. J., Ao, C. O., Li, K.: Estimating climatological planetary boundary layer heights from radiosonde observations:
515 Comparison of methods and uncertainty analysis, *J. Geophys. Res.-Atmos.*, 115, D16113, doi:10.1016/s1352-2310(99)003
516 49-0, 2010.

- 517 Seidel, D. J., Zhang, Y., Beljaars, A., Golaz, J.-C., Jacobson, A. R., Medeiros, B.: Climatology of the planetary boundary
518 layer over the continental United States and Europe, *J. Geophys. Res.-Atmos.*, 117, D17106, doi:10.1029/2012jd018143,
519 2012.
- 520 Song, Z. S., Zhu, B., Sun, G. W.: A preliminary study on the thermal mixing layer in the western Tibetan Plateau, the
521 Collected Works of the Tibetan Plateau Meteorological Scientific Experiment (Series 2), Beijing: Science Press, 253-261,
522 1984.
- 523 Stull, R. B.: An Introduction to Boundary Layer Meteorology, Springer Netherlands, doi:10.1007/978-94-009-3027-8, 1988.
- 524 Sun, F., Ma, Y., Li, M.: Boundary layer effects above a Himalayan valley near Mount Everest, *Geophys. Res. Lett.*, 34,
525 L08808, doi:10.1029/2007gl029484, 2007.
- 526 Tao, S. Y., Ding, Y. H.: Observational evidence of the influence of the Qinghai-Xizang (Tibet) Plateau on the occurrence of
527 heavy rain and severe convective storms in China, *Bull. Amer. Meteor. Soc.*, 62, 23-30, doi:10.1175/1520-0477(1981)062h
528 0023:OEOTIOi2.0.CO;2, 1981.
- 529 Wang, Y. J., Xu, X. D., Liu, H. Z., Li, Y. Q., Li, Y. H., Hu, Z. Y., Gao, X. Q., Ma, Y. M., Sun, J. H., Lenschow, D. H.,
530 Zhong, S. Y., Zhou, M. Y., Bian, X. D., Zhao, P., Wang, Y. J.: Analysis of land surface parameters and turbulence
531 characteristics over the Tibetan Plateau and surrounding region, *J. Geophys. Res. Atmos.*, 121, 9540-9560, doi:10.1002/
532 2016JD025401, 2016.
- 533 Xu, X., Bian, L., Zhang, G., Bian, L. G., Zhang, G. Z., Liu, H. Z.: A comprehensive physical pattern of land-air dynamic and
534 thermal structure on the Qinghai-Xizang Plateau, *Science in China Series D: Earth Sciences*, 45, 577-594, doi:10.1360/0
535 2yd9060, 2002.
- 536 Yanai, M., Li, C.: Mechanism of heating and the boundary layer over the Tibetan Plateau, *Mon. Wea. Rev.*, 122, 305-323,
537 doi:10.1175/1520-0493(1994)1222.0.CO;2, 1994.
- 538 Yang, K., Koike, T., Fujii, H., Tamura, T., Xu, X., Bian, L., Zhou, M. Y.: The daytime evolution of the atmospheric
539 boundary layer and convection over the Tibetan Plateau: observations and simulations, *J. Meteor. Soc. Japan*, 82, 1777-1792,
540 doi:10.2151/jmsj.82.1777, 2004.
- 541 Ye, D., Gao, Y. X.: The Meteorology of the Qinghai-Xizang Plateau, Beijing: Science Press, 89-101, 1979.
- 542 Yu, X. J., Du, J., Wang, M. Z., Xu, H. X., He, Q.: Impact of assimilating the new radiosonde data on Qinghai-Tibetan
543 Plateau on summer rainfall forecast over southern Xinjiang, *Plateau Meteor.*, 37(1), 13-27, doi:10.7522/j.issn.1000-
544 0534.2017.00034, 2018.
- 545 Zhang, G., Xu, X., Wang, J.: A dynamic study of Ekman characteristics by using 1998 SCSMEX and TIPEX boundary layer
546 data, *Adv. Atmos. Sci.*, 20, 349-356, doi:10.1007/bf02690793, 2003.
- 547 Zhang, Y., Seidel, D. J., Golaz, J.-C., Deser, C., Tomas, R. A.: Climatological characteristics of Arctic and Antarctic surface-
548 based inversions, *J. Climate.*, 24, 5167-5186, doi:10.1175/2011JCLI4004.1, 2011a.
- 549 Zhang, Q., Zhang, J., Qiao, J., Wang, S.: Relationship of atmospheric boundary layer depth with thermodynamic processes at
550 the land surface in arid regions of China, *Sci. China: Earth Sci.*, 54, 1586-1594, doi:10.1007/s11430-011-4207-0, 2011b.

- 551 Zhang, Q., Yue, P., Zhang, L., et al.: Land-atmosphere interaction over the summer monsoon transition zone in China: A
 552 review and prospects, *Acta Meteor. Sinica*, 77, 758-773, 2019.
- 553 Zhang, W., Guo, J., Miao, Y., Liu, H., Yang, S., Fang, Z., He, J., Lou, M. Y., Yan, Y., Li, Y., Zhai, P. M.: On the
 554 summertime planetary boundary layer with different thermodynamic stability in China: a radiosonde perspective, *J. Climate*,
 555 31, doi:10.1175/jcli-d-17-0231.1, 2017.
- 556 Zhao, C. L., Li, Y. H., Liu, Y. P., et al.: The variation characteristics of planetary boundary layer height in Northwest China:
 557 Based on radiosonde and ERA-Interim reanalysis data, *Plateau Meteor.*, 38, 1181-1193, doi:10.7522 /jissn.100005 34.2018.
 558 00152, 2019a.
- 559 Zhao, J. H., Zhang, Q., Wang, S.: A simulative study of the thermal mechanism for development of the convective boundary
 560 layer in the arid zone of Northwest China, *Acta Meteor. Sinica*, 69, 1029-1037, doi:10.11676/qxxb2011.090, 2011.
- 561 Zhao, M., Miao, M. Q.: The atmospheric boundary layer, Beijing: China Meteorological Press, 1992.
- 562 Zhao, P., Xu, X., Chen, F., et al.: The Third Atmospheric Scientific Experiment for understanding the earth-atmosphere
 563 coupled system over the Tibetan Plateau and its effects, *Bull. Amer. Meteor. Soc.*, 99, 757-776, doi:10.1175/BAMS-D-16-
 564 0050.1, 2018.
- 565 Zhao, P., Li, Y. Q., Guo, X. L., et al.: The Tibetan Plateau surface-atmosphere coupling system and its weather and climate
 566 effects: The Third Tibetan Plateau Atmospheric Science Experiment, *J. Meteor. Res.*, 33, 375-399, doi:10.1007/s13351-019-
 567 8602-3, 2019b.
- 568 Zhou, W., Yang, S. P., Jiang, X., et al: Estimating planetary boundary layer height over the Tibetan Plateau using COSMIC
 569 radio occultation data, *Acta Meteor. Sinica*, 76, 117-133, doi:10.11676/qxxb2017.069, 2018.



570

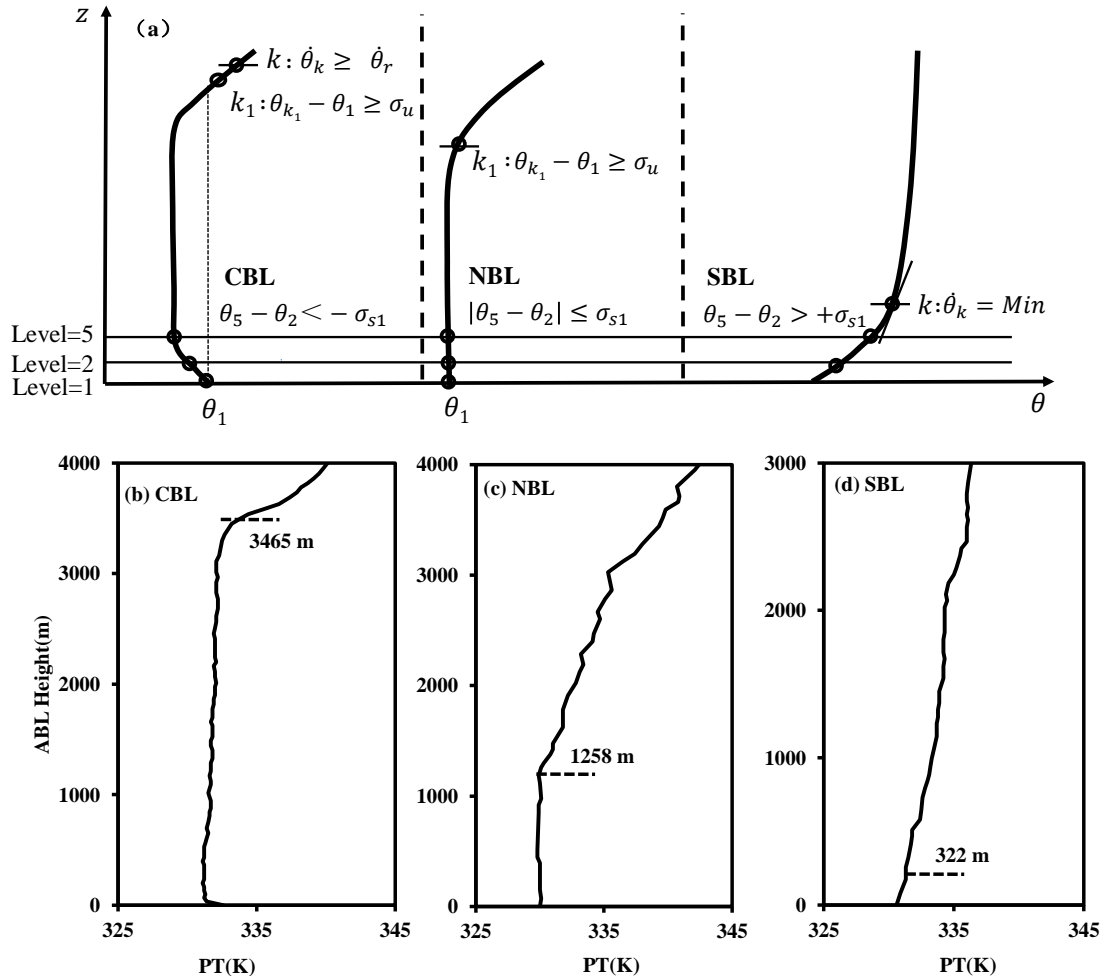
571 **Figure 1: Distribution of sounding stations, in which the number indicates sounding profiles at each station at (a) 08:00, 14:00, and**

572 20:00 BJT, (b) 08:00 BJT, (c) 14:00 BJT, and (d) 20:00 BJT in the study period. Red (black) dots represent intensive (operational)

573 observations. Some observation station names are given as abbreviations in (a) and the green line shows the 3000 m topography.

574

575



576

577

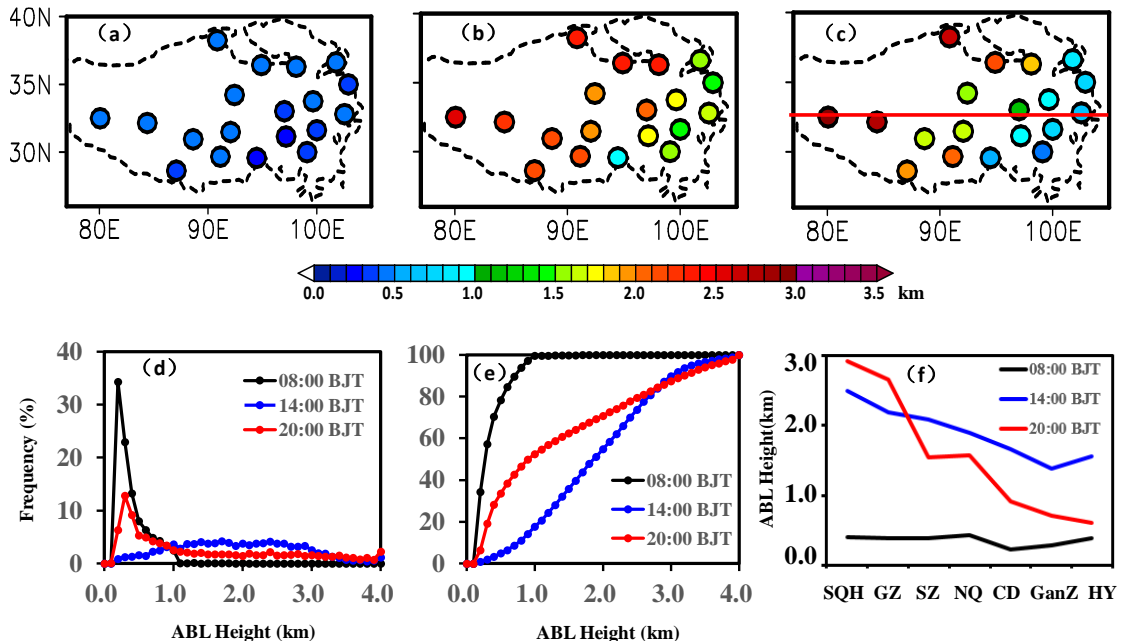
578 **Figure 2: (a) Illustration of the determination procedure for the convective boundary layer (CBL), neutral boundary layer (NBL),**

579 **and stable boundary layer (SBL) heights; and examples of the potential temperature (PT) profiles derived from sounding**

580 **observation at Lasa station at 20:00 BJT for (b) CBL on June 10, 2013, (c) NBL on July 21, 2013, and (d) SBL on August 11, 2013,**

581 **respectively. The dash line in (b)-(d) represents the ABL height identified using the algorithm described.**

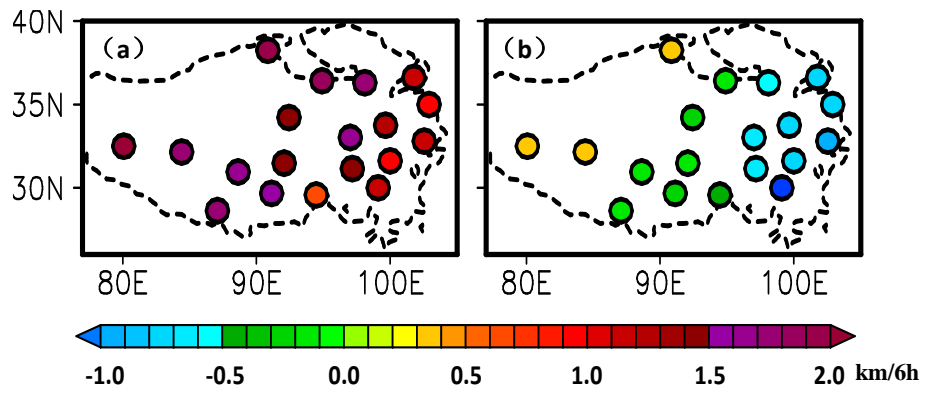
582



583

584 **Figure 3:** Spatial distribution of the mean ABL height (ABLH) at (a) 00:00 BJT, (b) 14:00 BJT, and (c) 20:00 BJT; (d) the regional
 585 mean frequency and (e) cumulative frequency distributions of the ABLH in the TP at 08:00 BJT, 14:00 BJT, and 20:00 BJT;
 586 (f) the west-east cross sections of the ABLH along 32°N (indicated by red line in (c)) at 08:00 BJT, 14:00 BJT, and 20:00 BJT.

587

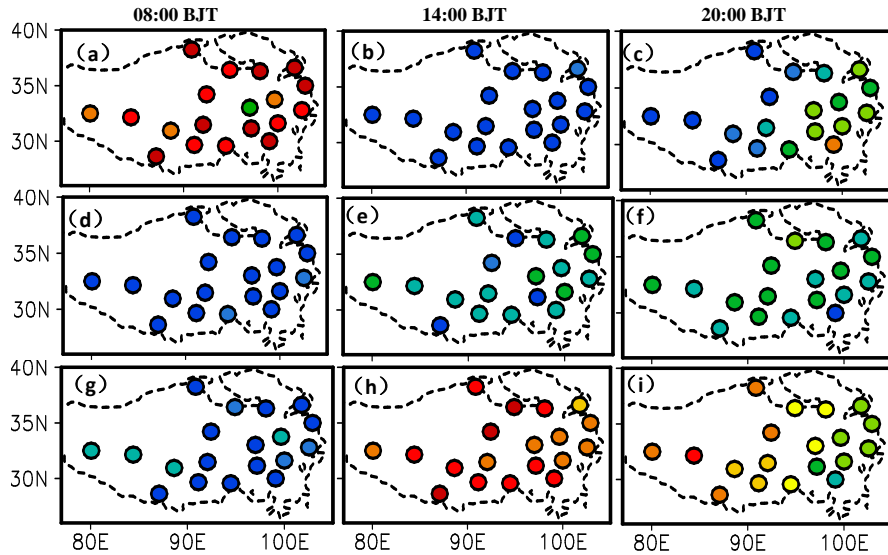


588

589

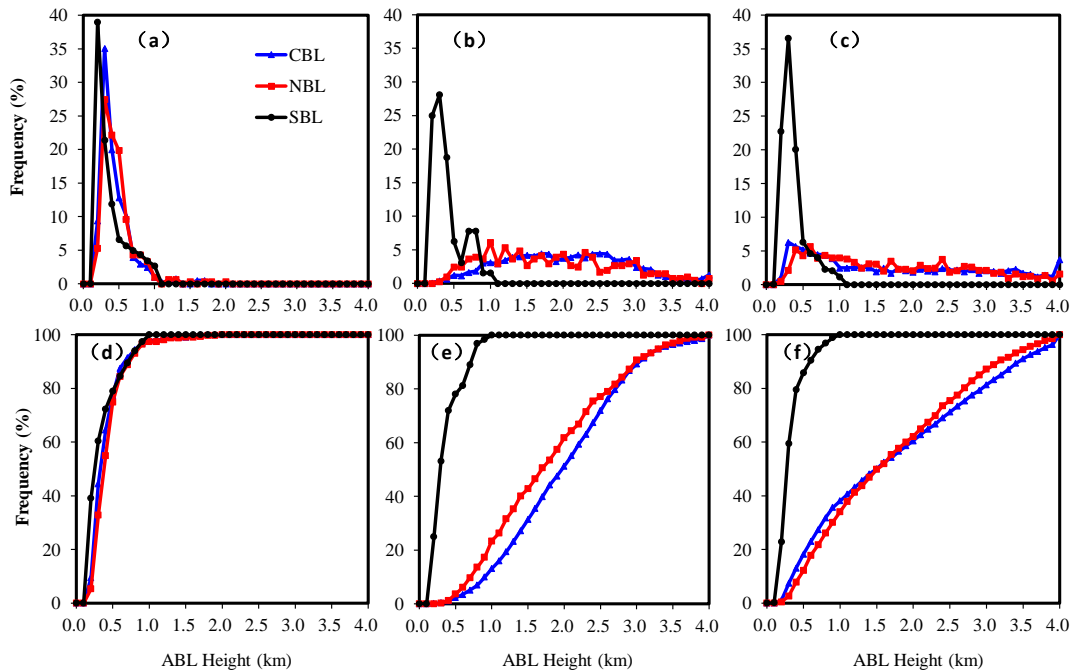
590 **Figure 4:** Spatial distribution of the ABLH growth rate from 08:00 BJT to 14:00 BJT (a) and from 14:00 BJT to 20:00 BJT (b).

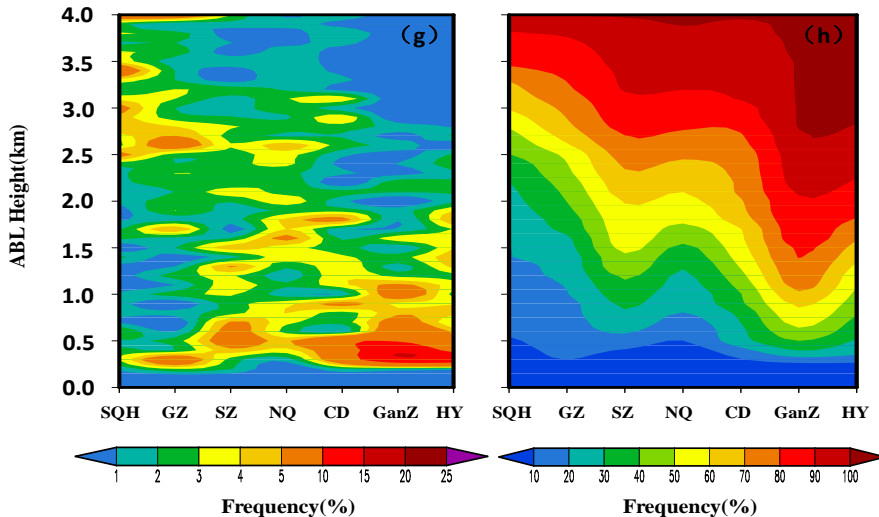
591



593

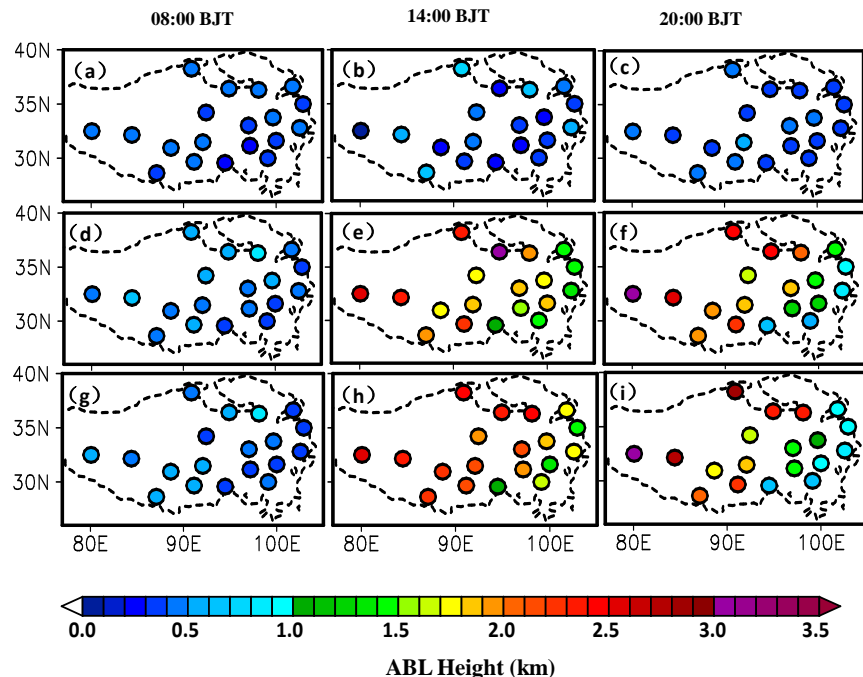
594 **Figure 5: Spatial distribution of the occurrence frequency for the SBL (top), NBL (middle), and CBL (bottom)**
 595 **at 08:00 BJT, 14:00 BJT, and 20:00 BJT.**





597

598 **Figure 6:** The regional mean frequency distributions of the ABLH over the TP for the CBL (blue), NBL (red), and SBL (black) at
 599 (a) 08:00 BJT, (b) 14:00 BJT, and (c) 20:00 BJT; and (d)-(f) same as in (a)-(c) but for the cumulative frequency distributions; and
 600 the west-east cross sections of frequency (g) and cumulative frequency (f) distributions of the CBL height along 32°N in the
 601 daytime (14:00 and 20:00 BJT).



602

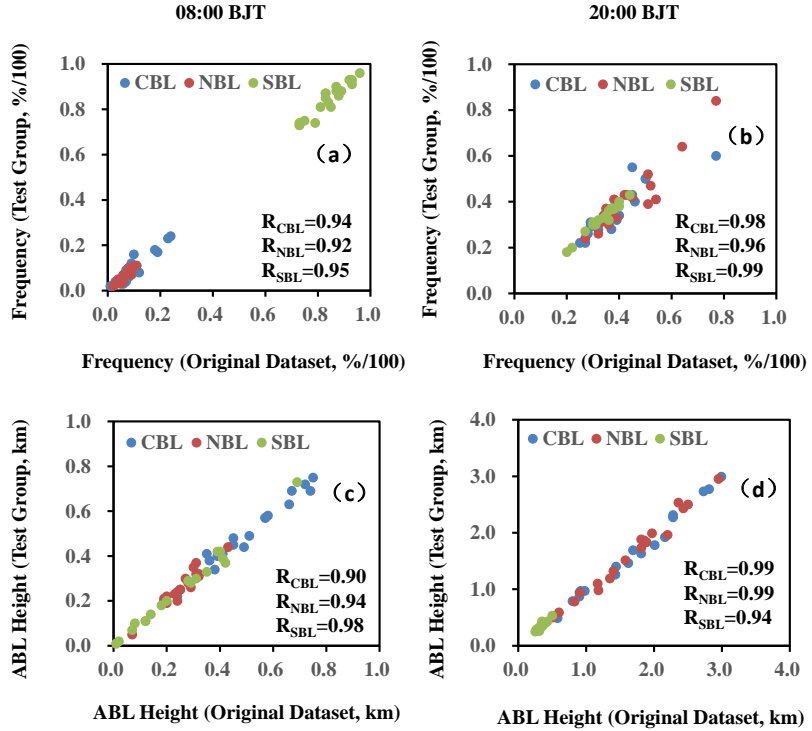
603

604 **Figure 7:** Spatial distributions of the mean ABLH for the SBL (top), NBL (middle), and CBL (bottom) at 08:00 BJT, 14:00 BJT,
 605 and 20:00 BJT.

606

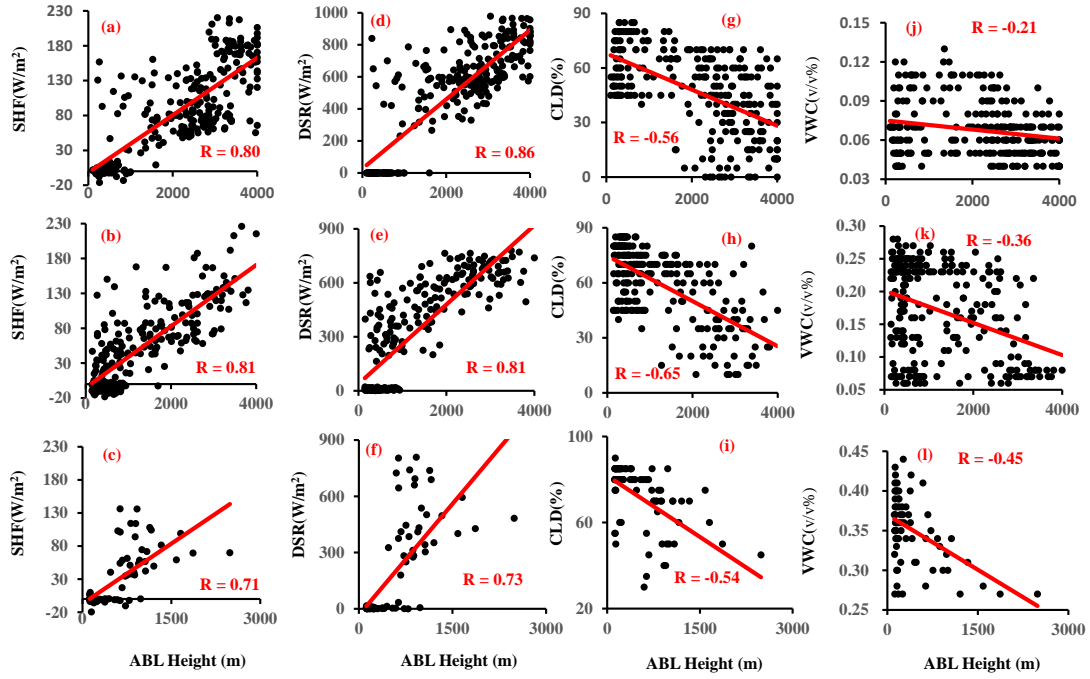
607

608



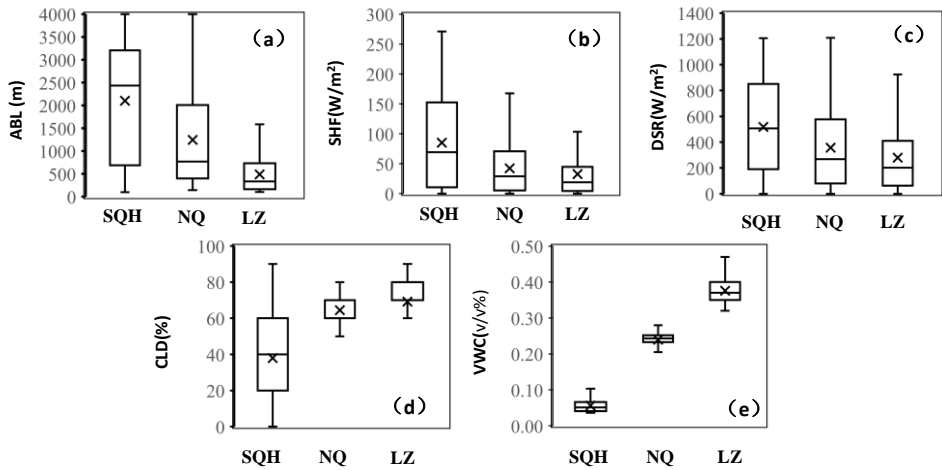
609

610 Figure 8: The scatter plots of occurrence frequency of the SBL, NBL, and CBL for the original and test group datasets at 19
 611 stations at (a) 08:00 BJT and (b) 20:00 BJT; and (c)-(d) same as in (a)-(b) but for the ABLH.



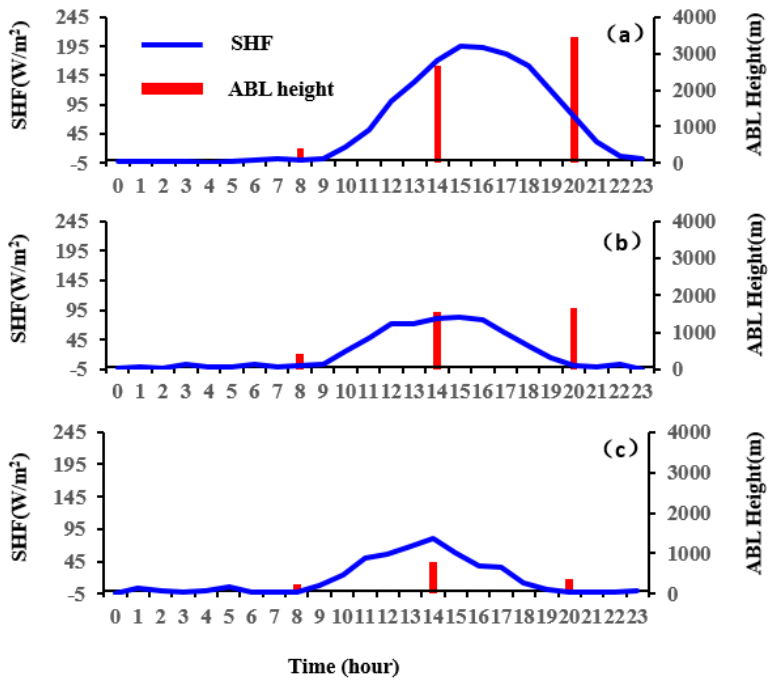
612

613 **Figure 9:** Scatter plots of the ABLH and the 6-hour average of surface sensible heat flux (SHF) (a-c), surface downward solar
 614 irradiance (DSR) (d-f), total cloud coverage (CLD) (g-i), and surface soil volume moisture content (VWC) (j-l) at 08:00 BJT, 14:00
 615 BJT, and 20:00BJT at SQH (top), NQ (middle), and LZ (bottom) stations in the study period. The correlation coefficient (R) is
 616 given in each panel.



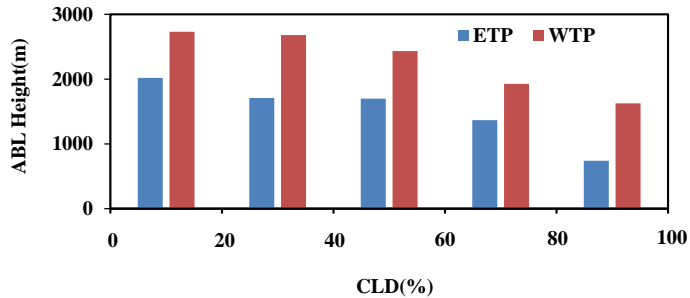
617

618 **Figure 10:** (a) The ABLH, (b) SHF, (c) DSR, (d) CLD, and (e) VWC at SQH, NQ, and LZ stations in the study period. Horizontal
 619 bars show the 5th, 25th, 50th, 75th, and 95th percentile values and “x” symbols show the corresponding mean value.



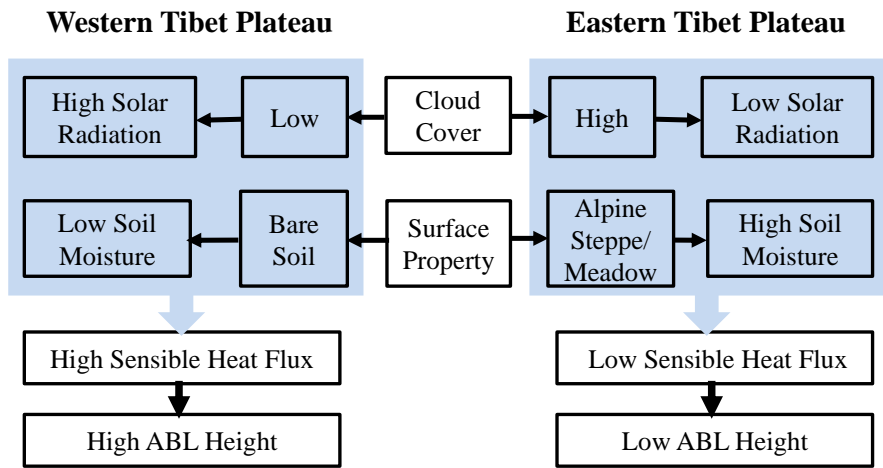
620

621 **Figure 11:** Diurnal variations of surface sensible heat flux (blue) and the ABLH (red) averaged over the study period at (a) SQH,
622 (b) NQ, and (c) LZ stations.



623

624 **Figure 12:** The mean ABLH (for the NBL and CBL) and CLD over the ETP (blue) and WTP (red) in the daytime (14:00 BJT and
625 20:00 BJT).



626

Figure 13: The schematic diagram for relationships between the ABLH and the influential factors in the ETP and the WTP.